

THE OLYMPIC MOUNTAINS EXPERIMENT (OLYMPEX)

ROBERT A. HOUZE JR., LYNN A. McMURDIE, WALTER A. PETERSEN, MATHEW R. SCHWALLER,
WILLIAM BACCUS, JESSICA D. LUNDQUIST, CLIFFORD F. MASS, BART NIJSSEN, STEVEN A. RUTLEDGE,
DAVID R. HUDAK, SIMONE TANELLI, GERALD G. MACE, MICHAEL R. POELLOT, DENNIS P. LETTENMAIER,
JOSEPH P. ZAGRODNIK, ANGELA K. ROWE, JENNIFER C. DEHART, LUKE E. MADAUS, AND HANNAH C. BARNES

OLYMPEX is a comprehensive field campaign to study how precipitation in Pacific storms is modified by passage over coastal mountains.

When frontal systems pass over midlatitude mountain ranges, precipitation is modified, often with substantial enhancement on the windward slopes and reduced accumulations on

the lee sides. Snow deposited at high elevations by these storms is an important form of water storage around the globe. However, precipitation over and near Earth's mountain ranges has long been very difficult to measure. As a result, the physical and dynamical mechanisms of enhancement and reduction of precipitation accompanying storm passage over mountains remain only partially understood. The launch of the Global Precipitation Measurement (GPM) satellite in February 2014 by the U.S. National Aeronautics and Space Administration (NASA) and the Japan Aerospace Exploration Agency (Hou et al. 2014) fosters exploration of precipitation processes over most of Earth's mountain ranges.

With its onboard Dual-Frequency Precipitation Radar (DPR) and 13-channel GPM Microwave Imager (GMI), the GPM satellite extends into future decades the global surveillance of precipitation provided until 2014 by the Tropical Rainfall Measuring Mission (TRMM) satellite and broadens coverage to higher latitudes, where many of Earth's snow-covered mountain ranges are located. GPM also serves as a reference for other satellites carrying a variety of microwave imaging or sounding radiometers [see Hou et al. (2014) for details]. It is therefore important to determine how accurately GPM instruments can determine rain and snowfall in storms passing over mountain ranges. To assess and improve the

AFFILIATIONS: HOUZE, McMURDIE, LUNDQUIST, MASS, NIJSSEN, ZAGRODNIK, ROWE, AND DEHART—University of Washington, Seattle, Washington; PETERSEN—NASA Marshall Space Flight Center, Huntsville, Alabama; SCHWALLER—NASA Goddard Space Flight Center, Greenbelt, Maryland; HOUZE AND BARNES—Pacific Northwest National Laboratory, Richland, Washington; BACCUS—Olympic National Park, Port Angeles, Washington; RUTLEDGE—Colorado State University, Fort Collins, Colorado; HUDAK—Environment and Climate Change Canada, King City, Ontario, Canada; TANELLI—Jet Propulsion Laboratory, California Institute of Technology, Pasadena, California; MACE—University of Utah, Salt Lake City, Utah; POELLOT—University of North Dakota, Grand Forks, North Dakota; LETTENMAIER—University of California, Los Angeles, Los Angeles, California; MADAUS—National Center for Atmospheric Research, Boulder, Colorado
CORRESPONDING AUTHOR: Robert A. Houze Jr., houze@uw.edu

The abstract for this article can be found in this issue, following the table of contents.

DOI:10.1175/BAMS-D-16-0182.1

In final form 15 February 2017

©2017 American Meteorological Society

For information regarding reuse of this content and general copyright information, consult the [AMS Copyright Policy](#).

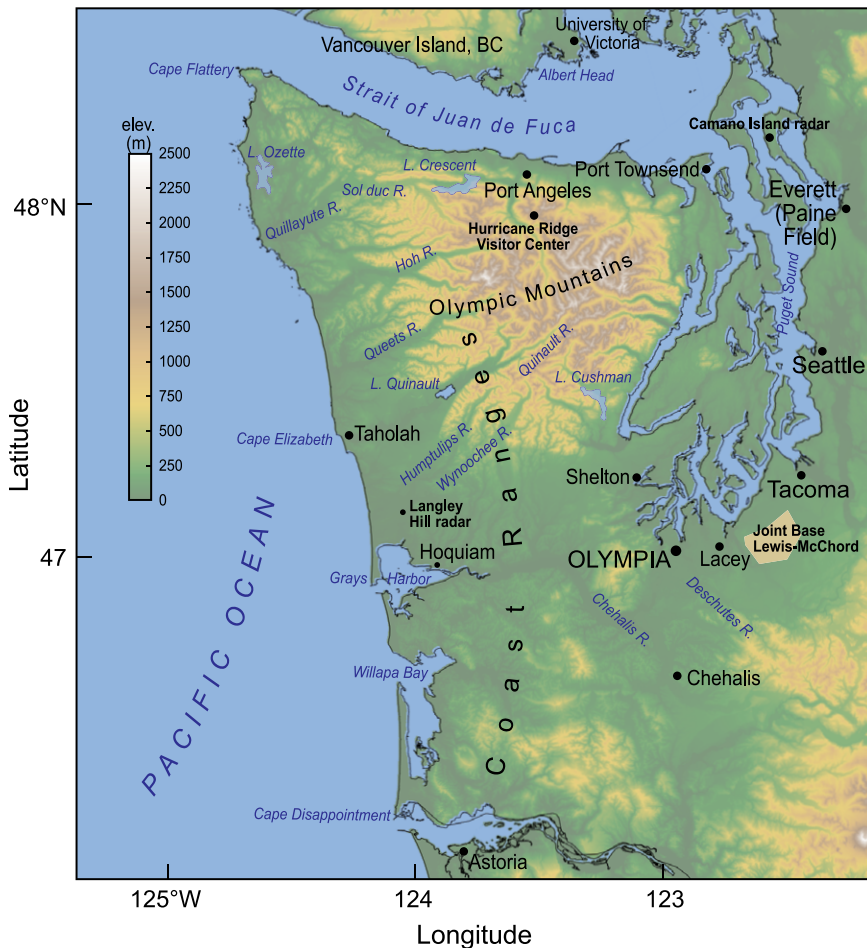


FIG. 1. Map of the region where the OLYMPEX campaign occurred, including the mountainous terrain of the Olympic Peninsula.

ability of the GPM satellite, the Olympic Mountains Experiment (OLYMPEX) was planned. OLYMPEX was an international, multiorganization field campaign¹ designed to collect detailed measurements by aircraft and ground sites to correspond with GPM satellite measurements over an area including a midlatitude mountain range with permanent snow cover. Figure 1 shows the terrain of the Olympic Mountain range, which occupies the Olympic Peninsula of the state of Washington. The peninsula has

¹ The organizations participating in OLYMPEX included NASA Goddard Space Flight Center, NASA Marshall Space Flight Center, Jet Propulsion Laboratory Caltech, Environment and Climate Change Canada, National Science Foundation, National Center for Atmospheric Research, Center for Severe Weather Research, National Park Service, National Weather Service, U.S. Forest Service, the Quinalt Indian Nation, Colorado State University, Texas A&M University, and the Universities of Illinois, Medellín (Colombia), Michigan, North Dakota, Utah, and Washington.

a north–south coastline on the Pacific Ocean and is separated from Canada’s Vancouver Island on its north side by the narrow Strait of Juan de Fuca.

The motivation for OLYMPEX was not only to better understand orographic modification of frontal precipitation processes but also to satisfy the need for further development and refinement of algorithms used to convert GPM’s satellite measurements to precipitation amounts in midlatitudes. The algorithms applied to TRMM satellite data over a nearly 17-yr period have been very successful for rain measurement and characterizing tropical convection (Simpson 1988; Simpson et al. 1996; Kummerow et al. 1998; Zipser et al. 2006; Huffman et al. 2007; Houze et al. 2015). However, these methods were designed for the warm tropical latitudes.

Microphysical processes producing precipitation are highly sensitive to the vertical profile of temperature, and an important characteristic of the tropics is that the horizontal temperature variation is slight. Therefore, relatively simple assumptions could be made about the horizontal structures of the cloud systems producing precipitation. The performance of satellite algorithms in baroclinic storm systems at midlatitudes presents new challenges because of the strong horizontal thermal gradients in extratropical cyclones and the disruption of storm structure by passage over mountain ranges.

The venue for OLYMPEX was chosen because it has precipitation from midlatitude baroclinic storm systems arriving frequently from the adjacent Pacific Ocean and abruptly transiting mountainous terrain. The western valleys and ridges of the Olympic Range are rain forests where these land-falling storms produce precipitation in amounts reaching 2,000–4,000 mm in a single season. Thus, climatologically and meteorologically the Olympic Peninsula was the ideal venue for this field

experiment. In addition, several airfields capable of serving large aircraft exist in the region, and the area of the Olympic Mountains is small enough that the OLYMPEX aircraft could fly in and over the incoming storms for long periods of time with minimal time spent traversing the distance to and from the observation site.

All of these factors made OLYMPEX an excellent venue to both better understand precipitation over mountains and improve satellite measurements of precipitation. More precisely stated, the OLYMPEX scientific strategy was two-fold: 1) collect a statistically robust set of measurements in midlatitude cyclones upstream of, over, and downstream of a mountain range that can be used to improve satellite algorithms² and 2) determine how the physics and dynamics of the precipitation mechanisms affect the satellite measurements through a detailed examination of the vertical structure of precipitating clouds. The second goal is of great benefit to meteorology in general, as it extends beyond satellite applications to address fundamental aspects of orographic effects on precipitation processes. This article will focus on the second, more general goal, illustrating how the OLYMPEX dataset presents an opportunity to improve basic understanding of mountain effects on precipitation. However, these two goals are strongly interrelated because the physical mechanisms producing precipitation determine

² OLYMPEX was led by NASA's GPM Ground Validation Program, whose goal is to validate assumptions in precipitation measurement algorithms. OLYMPEX benefited from a collaboration with the NASA Aerosols/Clouds/Ecosystem (A/C/E) Radar Definition Experiment (RADEX), which aims to improve multisensor cloud and precipitation property retrievals for the next generation of NASA satellite constellations.

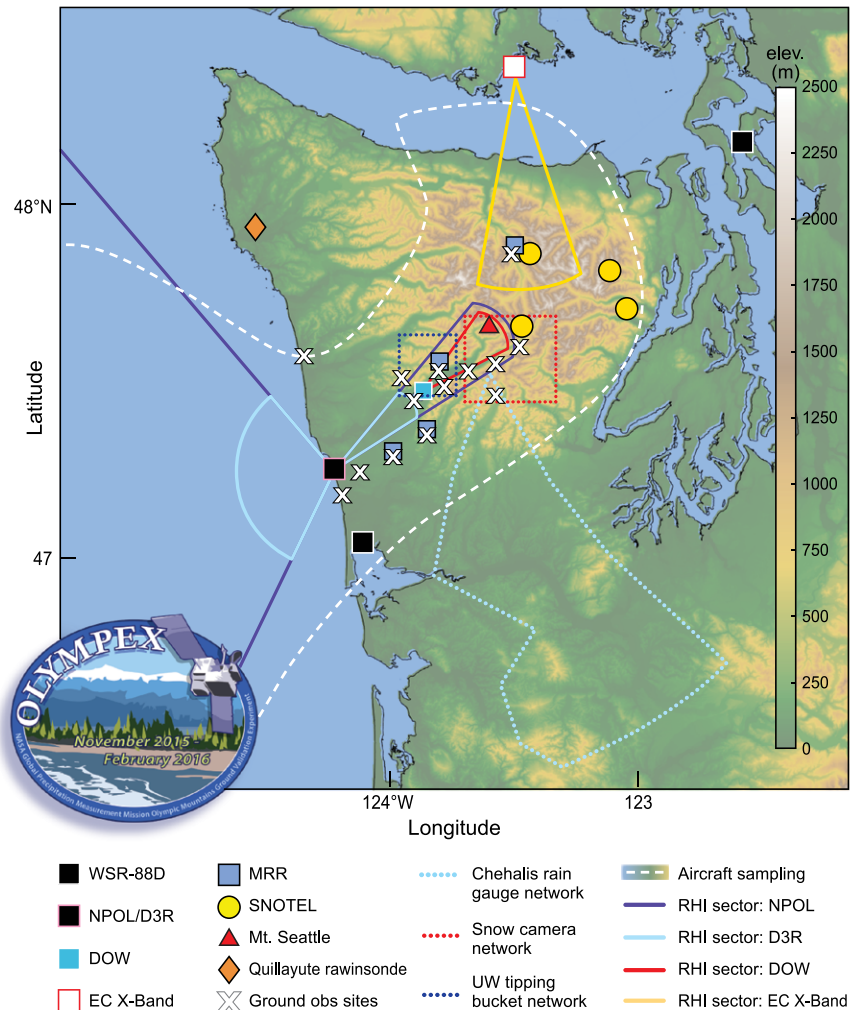


Fig. 2. The OLYMPEX observational network.

the vertical profiles of hydrometeors detected by the satellite, and the statistical datasets used to design and refine algorithms must be accurately stratified into physically homogeneous zones relative to both storm structure and terrain.

SETUP OF AN ADVANCED DATA COLLECTION PROGRAM IN A CHALLENGING VENUE.

The deployment of instruments and observations (Fig. 2) was designed to make measurements above, within, and below the clouds of extratropical cyclones passing over the windward slopes, high terrain, and lee side of the Olympic Mountains. Observations on the western side of the Olympic Peninsula were concentrated within and near the Quinault River valley, a very wet drainage on the windward side of the Olympic Mountains (Fig. 1). A secondary focus of observations was the Chehalis River valley lying to the south of the Olympic Mountains. On two occasions, when the primary

precipitation occurrence was in the Chehalis area, the OLYMPEX aircraft were diverted to this region (see “Examples of the OLYMPEX aircraft, radar, and surface data” section). Otherwise, aircraft missions focused on storm passages over the Olympic Mountains and were conducted primarily within the zone indicated by the white dashed contour in Fig. 2, which was centered on the Quinault River valley, the coastal zone upstream of the Quinault River valley, and the leeward region, including Hurricane Ridge, observed by the Environment and Climate Change Canada (EC) X-band dual-polarization radar on Vancouver Island.

Because overflights by the GPM *Core Observatory* only occur over any given location approximately two times per day, NASA aircraft (the DC-8 and ER-2, both with flight durations of 7–8 h) were used to mimic the satellite measurements by flying above cloud with onboard radars and passive microwave sensors similar to those on the satellite (Table 1). The DC-8 also launched dropsondes over the ocean to document upstream conditions. Coordinated with the high-altitude remote sensing aircraft was the University of North Dakota (UND) Citation aircraft, which flew primarily inside the clouds. It was equipped with state-of-the-art cloud microphysics

TABLE 1. List of instruments deployed on each aircraft and dates of operations.

Aircraft	Dates	Instrument	Purpose
DC-8 Flight altitude: 11.8 km	12 Nov– 19 Dec 2015	APR-3 radar	Ku-, Ka-, and W-band radar, Doppler (0.4 m s ⁻¹ precision) swath ±25°, 0.7–0.8-km footprint from 10-km altitude, sensitivity: ~0 dBZ (Ku), -17 dBZ (Ka)
		COSMIR radiometer	Passive microwave at 50, 89, 165.5, 183.3 ± 1, 183.3 ± 3, 183.3 ± 8 GHz. Cross-track/conical scan, 0.7-km footprint
		AVAPS dropsondes	T, Td, and wind profiles at locations over the ocean
ER-2 Flight altitude: 18 km	17 Nov– 14 Dec 2015	AMPR radiometer	Radiometer at 10.7, 19.35, 37.1, and 85.5 GHz; footprints 2.8, 2.8, 1.5, and 0.6 km, respectively, at 20 km
		HIWRAP radar	13.91 and 35.56 GHz (dual-pol LDR; nadir pointing); footprint ~1 km at 20 km
		EXRAD radar	9.4 (nadir) and 9.6 GHz (scanning; 25-km swath at 20-km altitude); footprint 1.2 km at 20 km
		CRS radar	94.15 GHz (nadir pointing); footprint ~0.16 km at 20 km
		AirMSPI radiometer	Eight-band radiometer (355, 380, 445, 470, 555, 660, 865, and 935 nm); push-broom scan, spatial resolution 10–25 m depending on scan mode
		CPL lidar	1,064 (50 μJ), 532 (25 μJ), and 355 (50 μJ) nm; 5-kHz PRF; footprint ~30 m at 20 km
Citation Flight altitude: 0.6–7.5 km	12 Nov– 19 Dec 2015	King hot wire probe	Liquid water, 0.02–5.0 g m ⁻³
		Cloud droplet probe (CDP)	Cloud droplet size distribution, 2–50-μm range
		2D-S	Particle images, 10–1,280 μm
		HVPS-3 (two units)	Particle images, 150 μm–1.92 cm; one horizontal and one vertically oriented instrument
		CPI	Cloud particle imager; particle imagery at 2.3-μm resolution
		CSI	Cloud water content, 0.02 to ~1.0 g m ⁻³
		2DC	Particle images, 30–960 μm
		Nevzorov	Total water content, 0.02 to ~1.5 g m ⁻³
Rosemount icing probe (RICE)	Supercooled water detection		
ASO	8–9 Feb 2016 and 29–30 Mar 2016	Lidar	Mapping of snow depth over the entire Olympic Mountain range

instrumentation and collected in situ observations of liquid and ice particle characteristics (particle images, phase, size distributions, and mass content) at a wide range of temperatures (see Table 1). GPM algorithms used to convert remote sensing measurements to precipitation mass concentration, fallout rates, and type depend on assumptions about the microphysical profile in the precipitating clouds as a function of temperature. Thus, the combination of aircraft used in the experiment provided for evaluation of the physics assumed in the algorithms applied to GPM measurements.

Coordinated with the aircraft observations was an extensive network of ground-based measurements (Fig. 2). Four state-of-the-art scanning dual-polarization Doppler radars, operating at several frequencies, observed the vertical and horizontal variability of hydrometeor characteristics and air motions within passing storms. The coastal radar site hosted the NASA dual-polarization S-band radar (NPOL) and the NASA dual-frequency (Ku/Ka band) dual-polarization Doppler (D3R) radar. The other two scanning radars were X band [the

National Science Foundation (NSF) Doppler On Wheels (DOW) and the EC X band] (Table 2; Fig. 2). The radar-scanning protocol was designed to maximize vertical sampling and resolution because of the following: 1) the GPM satellite radars have very fine vertical resolution (~0.25–0.5 km), and high vertical resolution is necessary for comparison to the satellite measurements; 2) a primary focus of OLYMPEX was to determine the microphysical processes upwind of and over the mountains, and the ice-phase microphysics active in these storms vary strongly in the vertical. In contrast, scanning of operational radars provides broad horizontal coverage from sequences of plan position indicator (PPI) azimuthal scans at a discrete set of elevation angles. OLYMPEX used the operational scans of the Langley Hill and Camano Island, Washington, National Weather Service (NWS) Weather Surveillance Radar-1988 Dopplers (WSR-88Ds) (Figs. 1 and 2) to provide the background horizontal mapping, while the OLYMPEX scanning radars operated in sectors in which range–height indicator (RHI) scans were executed at a discrete sequence of azimuth

TABLE 2. List of radars deployed along with their wavelengths and locations. All radars are Doppler dual-polarization except the MRRs and EXRAD, which are only Doppler.

Radar	Location	Frequency	Beamwidth (°)	Scanning mode				
NWS WSR-88D	Camano Island, WA	S band	0.88–0.96	Operational PPIs down to 0.5°				
	Langley Hill, WA	S band	0.88–0.96	Operational PPIs down to 0°				
NPOL	Near Taholah, WA	S band	0.94	RHI sectors interspersed with low-level PPIs				
D3R	Near Taholah, WA	Ku band	0.90	RHI sectors interspersed with low-level PPIs				
		Ka band	0.86					
EC X band	Albert Head, Vancouver Island, BC	X band	0.974	RHI sectors interspersed with low-level PPIs				
DOW	Lake Quinault	X band	0.95	RHI sectors up-valley interspersed with low-level PPIs				
MRRs	Hurricane Ridge Fish Hatchery Bishop Field Neilton Point	K band	2.0	Vertically pointing				
					Aircraft DC8	Ku band	3.8	Scans side to side relative to nadir
						Ka band	4.8	
						W band	5.4 (scanning)	
0.8 (nadir)								
HIWRAP	Aircraft ER-2	Ku band	3.1	Conical scanning around nadir, two Ka/Ku beams				
		Ka band	1.2					
EXRAD	Aircraft ER-2	X band	3.3	One nadir beam and a second beam scanning conically around nadir				
CRS	Aircraft ER-2	W band	0.45	Nadir pointing				



FIG. 3. Examples of the OLYMPEX surface observation sites. (a) Beach House site on the coast. (b) Mule train taking instruments to remote higher-elevation sites. (c) Installation of 2DVD (foreground) at the Fisheries site; dual-platform tipping-bucket gauge and Parsivel disdrometer are in the background. (d) University of Washington mobile trailer facility in the Wynoochee drainage. Photo credits: (a) Lynn McMurdie, (b) William Baccus, and (c),(d) Joe Zagrodnik.

angles (separated by 1° – 2°) to maximize the vertical resolution. The wedge-shaped areas in Fig. 2 show the areas in which the RHI scans were conducted in a constantly repeating cycle of ~ 20 min. The D3R was collocated with NPOL, but the latter had much greater range. As indicated in Fig. 2, the NPOL and D3R RHIs covered sectors over the ocean and the Quinault River valley, where most of the special surface observing sites were located. Because the NPOL beam was unable to reach into the valley at low levels owing to the beam's upward curvature and beam blockage by terrain, the DOW X-band radar was placed within the valley to extend the dual-polarization Doppler radar RHI coverage below the NPOL beam, down nearly to the valley floor. The EC X band was placed on Vancouver Island (Fig. 2)

in order to view the precipitation structure on the leeside of the Olympic Mountains and to coordinate with surface instrumentation placed at Hurricane Ridge ($\sim 1,600$ -m elevation; Fig. 1) within the Olympic National Park.

Within the areas of radar coverage, surface instruments were set up to measure rain and snow particle sizes and fall speeds as well as precipitation rates. The instruments at the sites shown in Fig. 2 and listed in Table 3 included various combinations of instruments, including pairs of tipping-bucket rain gauges (some with 0.3-m diameter catchment, others with 0.2-m diameter catchment) that recorded 0.254 mm per tip, Pluvio-2 weighing gauges, Micro Rain Radars (MRRs), and disdrometers. The types of disdrometers used included the Parsivel-2, the Two-Dimensional

TABLE 3. Locations of ground sites with multiple instrument deployments.								
Ground site	Location	Elevation (m)	Instruments					Dual (D) or single (S) rain gauge
			PIP and hot plate	2DVD	Parsivel	Pluvio	MRR	
Beach House	47.20°N, 124.2°W	4.6			x			D
Kalaloch	47.60°N, 124.37°W	11.9			x			D
Seed Orchard	47.27°N, 124.12°W	79.3			x			D
Fish Hatchery	47.36°N, 123.99°W	51.8		x	x		x	D
Neilton Point	47.39°N, 123.87°W	656.8	x	x	x	x	x	D
Amanda Park	47.46°N, 123.89°W	64.0		x	x			D
Norwood	47.49°N, 123.81°W	64.9			x			D
Bishop Field/CRN	47.51°N, 123.81°W	86.9		x	x		x	D
Prairie Creek	47.51°N, 123.93°W	542.5			x			D
Bunch Field	47.58°N, 123.68°W	115.8			x			S
Graves Creek	47.57°N, 123.58°W	180.8			x			S
Upper Quinault	47.67°N, 123.38°W	640.1			x	x		
Hurricane Ridge	47.97°N, 123.50°W	1,603	x		x		x	
Wynoochee Trailer	47.50°N, 123.58°W	1,018			x	x		

Video Disdrometer (2DVD), and a Precipitation Imaging Package (PIP). The ground sites were set up at various altitudes and distances from the scanning radars. Because of power availability and other logistical considerations, some sites could host only a subset of these instrument types. Table 3 does not include the locations where only rain gauges were deployed. In the area of the dark blue dotted rectangle in Fig. 2, a line of tipping-bucket gauges across the Quinault River valley and the ridge between the Quinault and Queets River valley to the north (Minder et al. 2008) provided the cross-ridge precipitation gradient. In the Chehalis area (light blue dotted polygon in Fig. 2), the conventional rain gauge network was supplemented with 10 dual tipping-bucket systems, which provided rainfall rates to supplement the conventional and cooperative networks. Wind shields for the rain gauges were not installed at the ground sites because of restrictions in wilderness areas. However, comparison of

one OLYMPEX gauge collocated with a permanent meteorological station with wind shielding yielded only a difference of 3%–5% in precipitation measurements during windy periods. A network of autonomous snow cameras (located within the red dotted rectangle in Fig. 2), viewing calibrated poles, gauged the change in snow depth throughout the season. During storm passages, environmental conditions were documented over land by supplemental rawinsondes launched at 2–6-h intervals from the NPOL

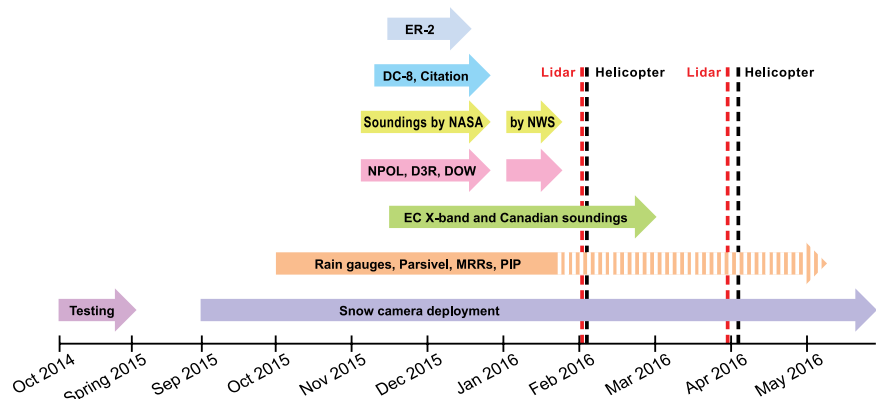


FIG. 4. Timeline of OLYMPEX operations. Solid arrows indicate periods when various facilities were in operation. Striped arrow shows the period in which the surface sites were reduced in number. Also indicated are the times that the ASO aircraft carried out lidar surveys of the snow cover in the Olympic Mountains (red dashed lines) and that crews were helicoptered into the high terrain to make measurements of snow depth (black dashed lines).

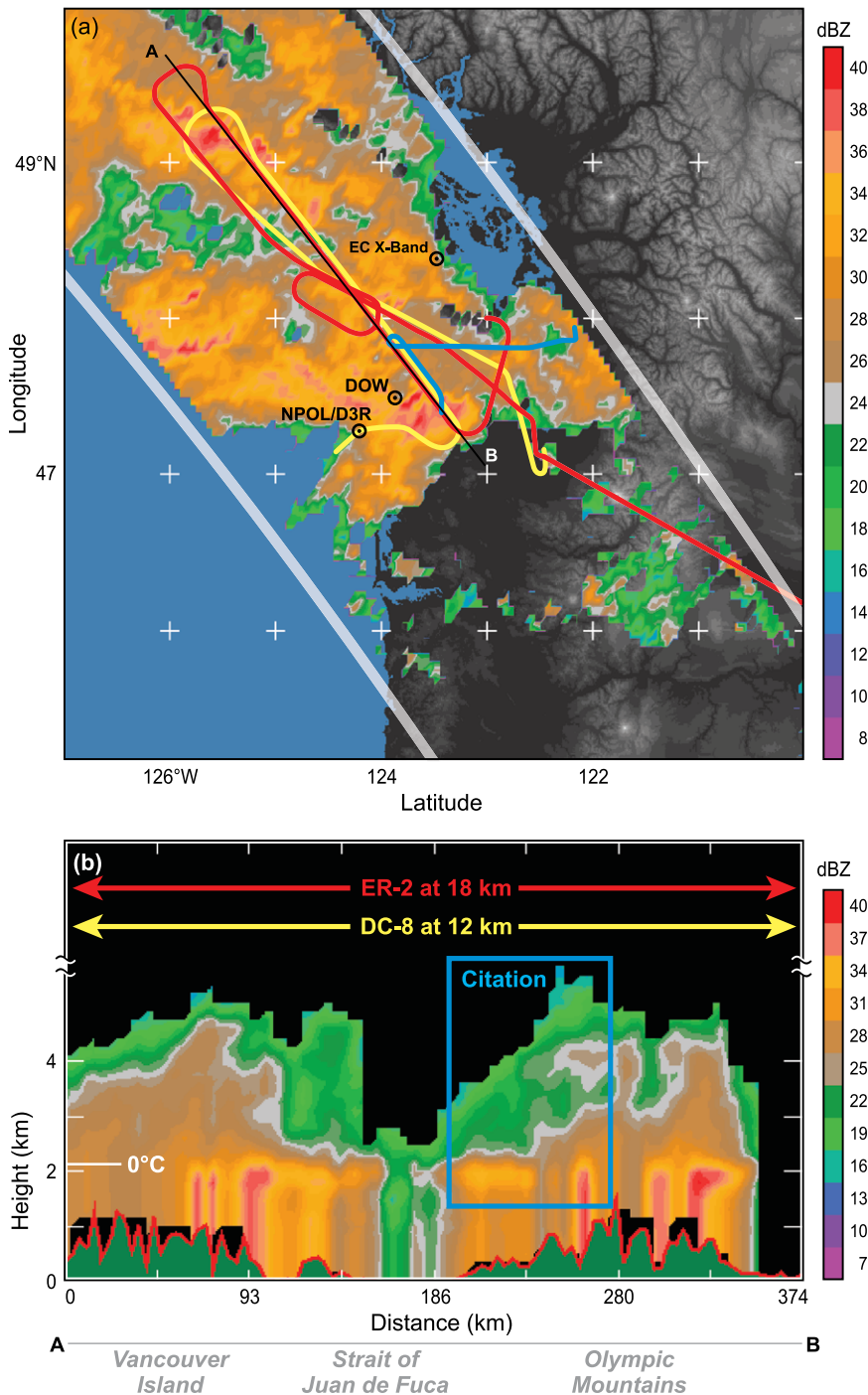


FIG. 5. Coordinated DC-8 (yellow), Citation (blue), and ER-2 (red) flights during ~1500–1600 UTC 3 Dec 2015 within the GPM satellite Ku-band radar swath. GPM overpass time 1522 UTC 3 Dec 2015. (a) Horizontal projection of Ku-band reflectivity and locations of ground-based radars. (b) Vertical cross section of GPM Ku-band along the black line in (a), showing flight altitudes, 0°C level, and underlying topography (dark green).

site and the University of Victoria on Vancouver Island (see Fig. 2 for locations) and over the ocean by dropsondes from the DC-8.

OLYMPEX had many key participants in addition to those who contributed directly to this paper as coauthors (see acknowledgments).

Despite the meteorological and climatological suitability of the Olympic Peninsula for this project, the wilderness of the Olympic Mountains and surrounding terrain was a challenging venue for a field experiment. The Olympic National Park, National Forests, and Quinault Nation land occupy most of the region. Rugged terrain, tall trees, primitive roads and trails, and lack of accessible electric power were primary obstacles to setting up the observational sites. Figure 3 shows several of the instrument sites and the mule train carrying instruments to the most remote sites. Despite these challenges, the radars and surface sites were successfully installed, with crucial assistance and cooperation from the National Park Service, the Quinault Indian Nation, and the Canadian Department of National Defense. In the end, the radars operated without significant blockage by trees or terrain, and ran continuously without major interruptions. Doggedly determined maintenance by ground crews traveling by foot through difficult and often dangerous terrain in all weather conditions kept the ground instruments working nearly continuously over the several months of the project, although some interruptions due to flooding, strong winds, and heavy snowfall were inevitable.

TIMELINE OF THE CAMPAIGN.

OLYMPEX field activity was carried out over a period of nearly two years. Figure 4 shows that a period of testing started in October 2014 and continued through the winter of 2014/15. At Snoqualmie Pass in the Cascade Mountains, surface instruments and battery/solar power configurations were tested. A Parsivel-2 disdrometer and a Pluvio-2 400 weighing precipitation gauge were mounted on a trailer with power supplied by solar panels that charged a bank of batteries.

Figure 3d shows the trailer as it was deployed in OLYMPEX. A Parsivel-2, PIP, hotplate, and MRR were installed and successfully tested at Hurricane Ridge (Fig. 1). Snow pole and camera installations were also tested in 2014–15.

Figure 4 shows the actual experiment beginning in September 2015, when the snow camera installation was completed. Rain gauges, Parsivel-2s, MRRs, and PIPs were installed throughout the month of October and all were fully operational by early November. At the end of January, some but not all of the ground instruments were removed. The scanning radars (NPOL, D3R, DOW, and EC X band)

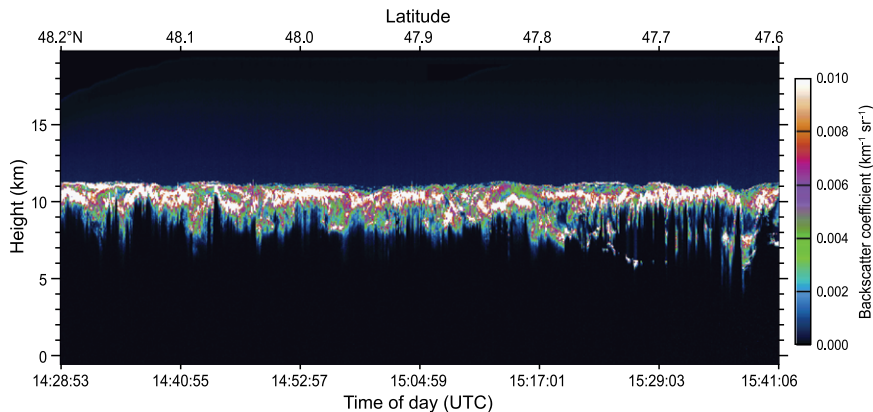


FIG. 6. Attenuated backscatter shown by the 532-nm cloud physics lidar (CPL) aboard the ER-2 on 3 Dec 2015. Time is in UTC and height in km. Since the scattering cross section of cloud-top ice crystals is approximately twice their physical cross section, the CPL is very sensitive to the precise location of cloud top. The strength of the signal tends to penetrate approximately 3–3.5 optical depths, providing an approximate indication of the density of hydrometeors in the cloud-top region.

operated through mid-January (with a Christmas break for the U.S. radars) except for the EC X-band, which continued until March. Supplemental soundings were taken at the NASA NPOL and UV sites until the December holiday break and at the NWS Quillayute site during the first half of January. The aircraft flew science missions from 12 November to 21 December 2015. The pyramid of arrows in Fig. 4 illustrates how the observations were nested in time, peaking in the November–December period.

On 8–9 February and 29–30 March, assessments of snowpack accumulation during the winter in the Olympic Mountains were made by airborne lidar aboard the Jet Propulsion Laboratory’s Airborne Snow Observatory (ASO) aircraft (Painter et al. 2016) and by crews carried by helicopter to measure the depth and density of the snowpack. The manual snow surveys were conducted near most of the locations of the snow poles and cameras. The lidar measurements were compared to data obtained on an earlier flight conducted in September 2014 with no snow cover on the mountains to determine the snow depth. The February flights occurred at a mid-season time before maximum snow cover. The late March flights took place when winter snow cover was near maximum.

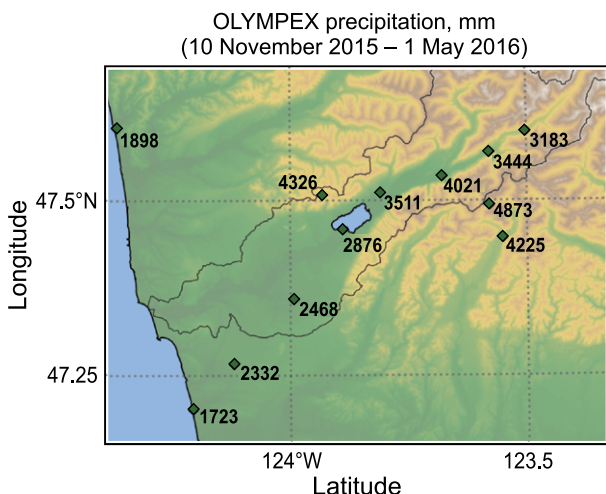


FIG. 7. Total accumulated liquid water equivalent precipitation at OLYMPEX ground sites from 10 Nov 2015 through 1 May 2016. The elevation scale is as in Figs. 1 and 2.

SUCCESSFUL PROJECT COORDINATION.

OLYMPEX operations required careful coordination of forecasting, decision-making, and scheduling of aircraft, radars, and soundings. The success of OLYMPEX operations is perhaps best illustrated in Fig. 5 showing how all three aircraft were positioned in the center

TABLE 4. List of storms sampled by aircraft during OLYMPEX. Other storms sampled by ground-based instrumentation and radars that occurred before, during, and after these systems are not included. (The nonaircraft cases and further details of the aircraft cases are described at <http://olympex.atmos.washington.edu>.)

Dates	Synopsis	Flights (UTC; to nearest 15 min)	Sectors sampled
12 Nov	Very warm, very moist atmospheric-river-type storm. GPM overpass.	DC-8: 1600–2200 Citation: 1930–2230	Prefrontal, warm sector
13 Nov	Continuation of same system with NCFR passage at 2300 UTC 13 Nov.	DC-8: 1400–1920 Citation: 1500–1745	Warm sector, cold front
14 Nov	Surface low offshore with frontal wave activity. Warm sector rain contributed to Chehalis flooding. GPM overpass.	DC-8: 1700–2315 Citation: 1945–2230	Warm sector, frontal wave
18 Nov	Weak postfrontal showers early in period, followed by overrunning mid- to high-level clouds that produced stratiform precipitation.	DC-8: 1830–0000 ER-2: 1800–0000 Citation: 2130–0000	Postfrontal, overrunning precipitation, and prefrontal sector
23 Nov	Weakening cold-frontal passage with relatively low melting level.	DC-8: 1530–2200 ER-2: 1400–2215 Citation: 1500–1800, 2030–2330	Prefrontal conditions, frontal precipitation
24 Nov	Postfrontal showers and cold-air outbreak behind weak frontal system from previous day.	DC-8: 1345–2015 ER-2: 1500–2215 Citation: 1615–1745, 1845–2145	Orographic precipitation over Hurricane Ridge and postfrontal showers offshore
25 Nov	Clear-air calibration flight for DC-8.	DC-8: 1645–1930	Clear air
1 Dec	Weakening storm with broad stratiform region and orographic enhancement.	DC-8: 2100–0145 ER-2: 2100–0200 Citation: 2245–0145	Prefrontal, warm sector, some frontal waves
3 Dec	Complex relatively warm system with multiple frontal waves and orographic enhancement on the south slopes of the Olympic Mountains. GPM overpass.	DC-8: 1430–1730 ER-2: 1415–1730 Citation: 1400–1700	Prefrontal, warm sector, frontal waves
4 Dec	Postfrontal convection behind the 3 Dec storm system with some deeper mesoscale cloud bands.	DC-8: 1300–1800 ER-2: 1300–2000 Citation: 1300–1600, 1700–2000	Postfrontal
5 Dec	Pacific frontal system with initially low melting heights but rising with warm advection.	DC-8: 1345–1900 ER-2: 1345–1800 Citation: 1445–1800	Prefrontal and warm sector
8 Dec	Large atmospheric river event with flooding on Quinault and then the Chehalis. GPM overpass.	DC-8: 1300–2030 ER-2: 1830–0030	Prefrontal, warm sector, and frontal waves
10 Dec	Occluded-frontal passage and widespread postfrontal showers.	DC-8: 1445–2000 ER-2: 1600–2200 Citation: 1445–1700	Postfrontal
12 Dec	Pacific frontal system with a warm sector and occluded front over the OLYMPEX region.	DC-8: 1545–2145 ER-2: 1800–2200 Citation: 1700–2015	Prefrontal, warm sector, and frontal
13 Dec	Postfrontal showers following occluded front of 12 Dec.	DC-8: 1345–1845 ER-2: 1600–0000 Citation: 1545–1915, 2000–2315	Postfrontal
18 Dec	Complex occluded front with convective elements in the prefrontal and postfrontal environments.	DC-8: 0445–0730 Citation: 0115–0430, 0545–0845	Prefrontal and frontal
19 Dec	Postfrontal convection following occluded front of 18 Dec. GPM overpass.	DC-8: 0130–0345 Citation: 0100–0400	Postfrontal

of a GPM overpass at 1522 UTC 3 December 2015. The background image is the GPM Ku-band radar reflectivity, and the three aircraft were flying patterns inside the GPM Ku-band radar swath. Figure 5b shows the altitudes of the aircraft in relation to the vertical cross section through the GPM radar reflectivity data obtained along the parallel flight tracks of the ER-2, DC-8, and Citation. The ER-2 was located at an altitude of 18 km, well above the 12-km cloud tops detected by the ER-2 CPL lidar (Fig. 6). These lidar measurements are especially important because they are the one way we had to determine the heights of the tops of the clouds in OLYMPEX. The DC-8 was flying near the 12-km level but well above the radar-echo layer seen by GPM. Both the ER-2 and DC-8 operated their radar and passive microwave instruments pointed downward to receive data similar to that collected by the satellite. At the same time, the Citation flew within the clouds at altitudes ranging from 1.5 to 6 km and obtained data on the sizes and other characteristics of the liquid and ice particles within the layer of radar echo.

WEATHER: COPIOUS PRECIPITATION FROM A SUCCESSION OF STORMS. OLYMPEX benefited from cooperative weather providing great amounts of precipitation from a series of synoptically well-defined storms. Figure 7 shows the precipitation accumulations recorded by the OLYMPEX gauges in the Quinault region for most of the cold season (10 November 2015–1 May 2016). Amounts were 1,700 to 4,900 mm. Importantly for this project, these amounts showed a systematic increase from a minimum on the coast to a maximum in the Quinault valley midway up the windward side of the Olympics, an enhancement of nearly a factor of 2.5 over a distance of ~50 km. The highest amounts were recorded at the higher-elevation sites surrounding the Quinault valley.

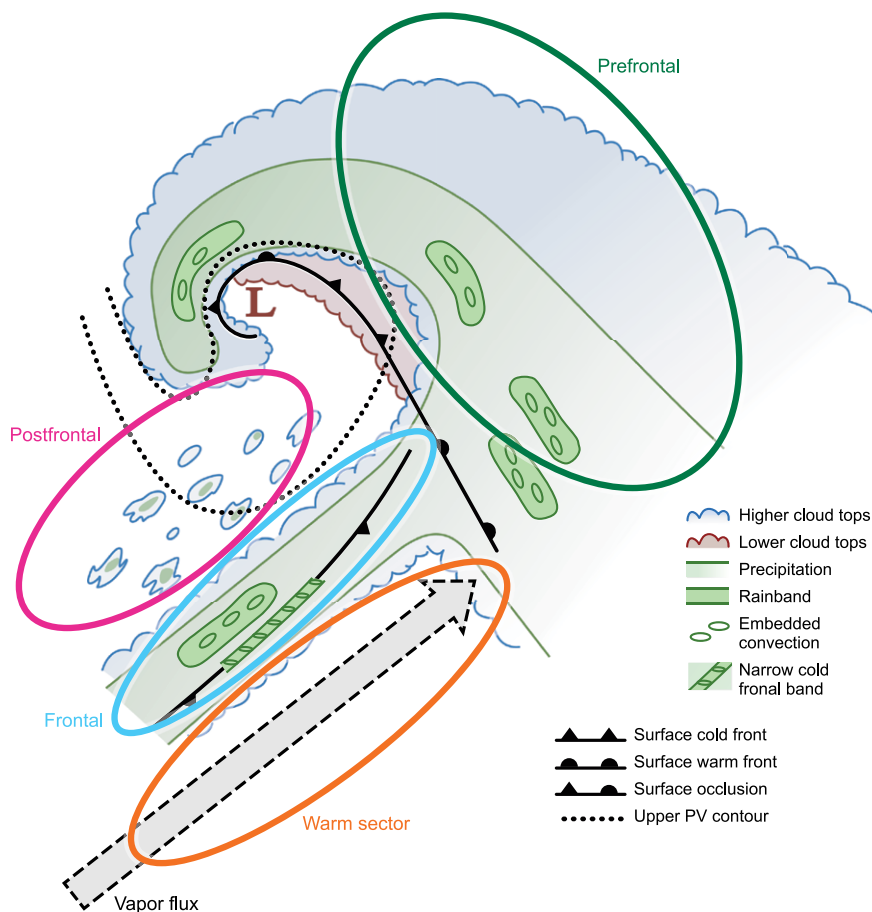


FIG. 8. Idealization of the sectors of a typical extratropical cyclone passing over the OLYMPEX region. Modified from Houze (2014).

A total of 11 Pacific frontal systems were sampled by aircraft (Table 4) with additional storms sampled by the radars and ground network (for more details on all cases sampled see http://olympex.atmos.washington.edu/index.html?x=Science_Summaries). These storms have a well-known characteristic structure (Nagle and Serebreny 1962; Houze et al. 1976; Matejka et al. 1980; Houze and Hobbs 1982; Medina et al. 2007; and others). This idealized storm structure (Fig. 8) guided daily forecast and planning of OLYMPEX operations. Storms are divided into four basic sectors: prefrontal, warm sector, frontal, and postfrontal. In real storms, these sectors are sometimes hard to distinguish precisely. Nevertheless, over the course of OLYMPEX, each sector was sampled. A summary of the aircraft sampling is in Table 4.

The storms that moved across the Olympic Mountains during the period of most intensive OLYMPEX observations did so within a hemispheric flow regime that was slowly evolving as shown in Fig. 9.

The 10–20 November period (Figs. 9a,b) was wet, characterized by nearly westerly mean flow toward

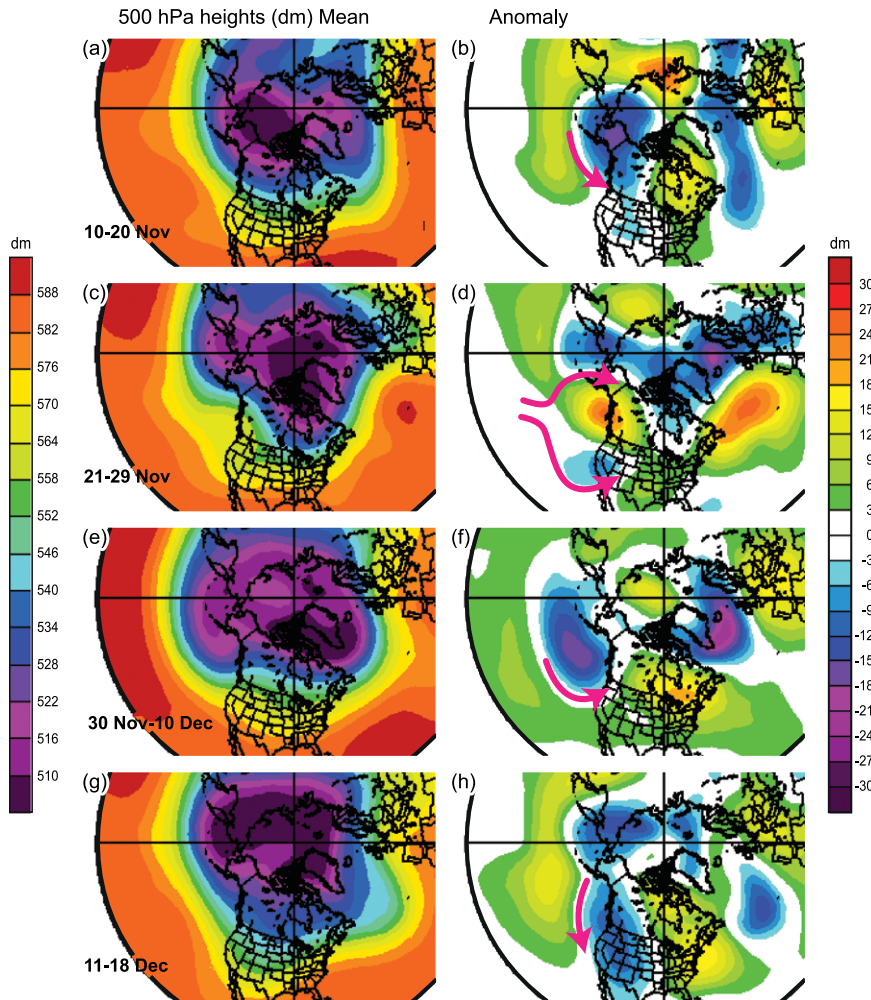


FIG. 9. (left) Mean and (right) anomaly heights of the 500-hPa surface during four subperiods of OLYMPEX. Pink arrows indicate anomalous flow pattern at that level. The anomalies were calculated by subtracting the mean flow from the 30-yr climatology of the same time period. This figure was constructed from the NCEP–NCAR reanalysis dataset (Kalnay et al. 1996), and the images were provided by the NOAA/ESRL/Physical Sciences Division, Boulder, Colorado, from their website (www.esrl.noaa.gov/psd/).

the OLYMPEX area. Twice, on 13 and 17 November, Lake Quinault rose at a rate of 0.15 m h^{-1} for 12–18 h and nearly flooded the DOW radar site on the shore of the lake (Figs. 1 and 2). These two storms were “atmospheric rivers,” in which long plumes of moisture in the warm sector just ahead of the cold front are advected by the low-level jet ahead of the front. When this moisture plume intersects the mountains, great enhancement of the frontal precipitation occurs (Neiman et al. 2008; Houze 2012, 2014).

After this exceptionally stormy period, a ridge persisted over the OLYMPEX region during 21–29 November. Anomalously strong split flow directed storm activity to the north and south of the region (Figs. 9c,d). The clear skies allowed a DC-8 flight to

determine the backscattering cross section and microwave emissivity of Earth’s surface under cloudless conditions, which must be known to accurately interpret airborne and satellite remote sensor measurements when clouds and precipitation are present.

From 30 November to 10 December strong southwesterly flow brought vigorous storms into the OLYMPEX region (Figs. 9e,f). The Wynoochee trailer site recorded over 1,000 mm of precipitation. The 3 December storm, in which the satellite and aircraft coordination were nearly perfect (Fig. 5), occurred during this period. On 8–9 December, another atmospheric river passed over the region. Figure 10 presents model output showing the 3-hourly precipitation accumulation forecast valid 1800 UTC 8 December. Note the strong enhancement of the precipitation on the windward ridges of the Olympic Mountain range. During this storm, the DOW site on Lake Quinault was again nearly flooded (Fig. 11).

After 10 December, the weather turned colder. The mean flow from 11 to 18 December was west-northwesterly with anomalous trough conditions over the Northwest (Figs. 9g,h). This regime features frontal system passages dominated more by ice-phase microphysics and incidences of postfrontal convection.

The four regimes illustrated in Fig. 9 were each ~10 days in duration and thus provided a nearly ideal set of storms for the aircraft to sample in each period (Fig. 4). After December, the OLYMPEX radars and ground instruments continued to operate. Much of early January was dominated by a split flow pattern, somewhat similar to Figs. 9c,d; as a result, only two weak storm systems were observed. Many of the surface instruments remained in operation through

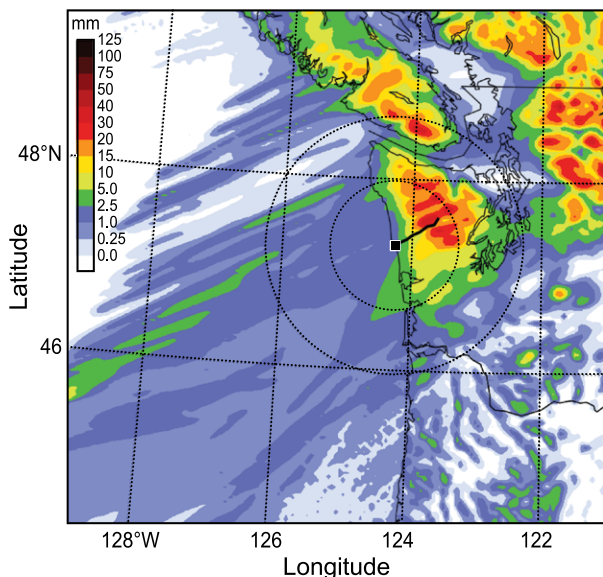


FIG. 10. Six-hour forecast of the precipitation accumulation for 1500–1800 UTC 8 Dec 2015 from the real-time University of Washington version of the Weather Research and Forecasting Model (Skamarock et al. 2008). Black box indicates NPOL/D3R location with NPOL range rings at 50 and 100 km (dashed). Black line indicates Quinault River valley.

the winter, and the helicopter and lidar snow surveys assessed the final snow cover at the times indicated in Fig. 4.

EXAMPLES OF THE OLYMPEX AIRCRAFT, RADAR, AND SURFACE DATA: UNPRECEDENTED DETAILS OF THE PRECIPITATION PROCESSES IN WEST COAST FRONTAL SYSTEMS. OLYMPEX exceeds many previous meteorological field campaigns, especially those conducted on the West Coast, in the variety of instrumentation and level of technology deployed. In this section we present examples of each of the data types.

Figure 12 illustrates data collection for a storm that contained a narrow cold-frontal rainband [NCFR; see Houze (2014, chapter 11) for a discussion of this type of band]. The NCFR was marked by the line of

high reflectivity seen approaching NPOL from the west in Fig. 12a. Soundings were scheduled immediately ahead of and behind the line (Figs. 12b,c). The frontal inversion and the rapid shift of surface wind from southwest to northwest are clearly seen in the sounding after the line’s passage. Three such NCFRs were observed in OLYMPEX.

One of the most important features of OLYMPEX was its variety of radar measurements showing vertical structures of storms. Figure 13 illustrates measurements with the Airborne Third Generation Precipitation Radar (APR3) triple-wavelength radar system aboard the DC-8 aircraft. The Ku- and Ka-band frequencies emulate the GPM satellite radar measurements. The W band provides further insight into the precipitation processes because of its ability to detect smaller particles. Because the DC-8 flew above the precipitation layer and for long distances, it documented the variation in radar echo structure between windward (Fig. 13, left side) and lee (Fig. 13, right side) slopes of the Olympic Mountains. The bright band at the melting level is clearly apparent at 2–3-km altitude in the Ku- and Ka-band reflectivity. Before about 1707 UTC, these two frequencies also showed low-level echo enhancement over the windward slopes and downward sloping of the bright band over the higher terrain. Marwitz (1987) and Minder et al. (2011) suggest the sloping melting level could be due to latent cooling from melting snow, the distance over which the hydrometeors melt, adiabatic cooling from forced lift of air over the barrier, or some combination. After ~1707 UTC, the APR-3



FIG. 11. Dr. Joshua Wurman of Center for Severe Weather Research at the DOW radar site on 9 Dec 2015. Photo credit: Alycia Gilliland.

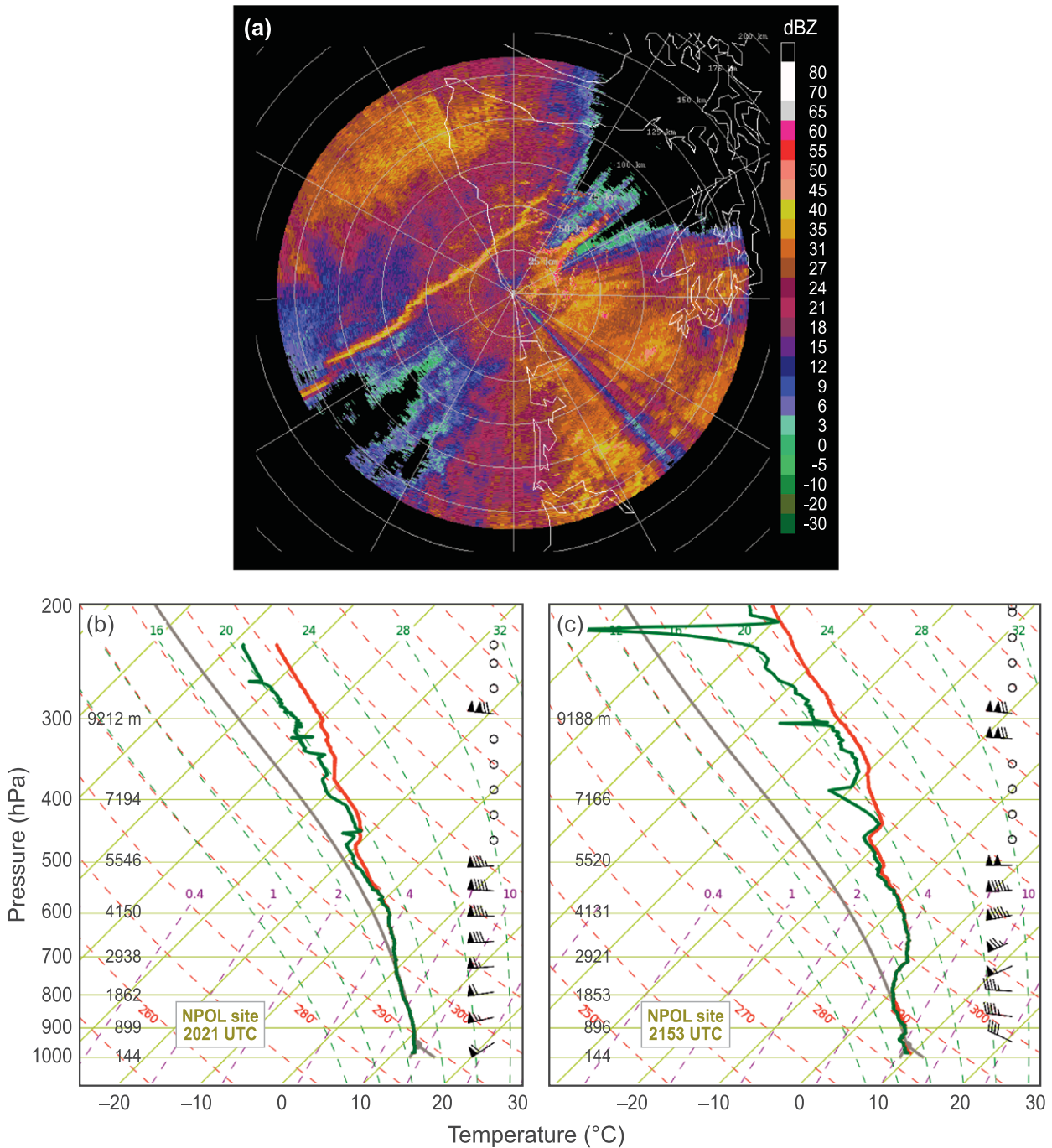


FIG. 12. (a) NPOL radar reflectivity showing approaching NCFR at 2032 UTC 17 Nov 2015. Range rings (white) are at intervals of 25 km. (bottom) Data from soundings launched from the NPOL site (b) before (2021 UTC) and (c) after (2153 UTC) passage of the NCFR.

frequencies show absence of low-level enhancement and an overall decrease in echo in the leeside “rain shadow” zone.

The NPOL S-band dual-polarization Doppler radar obtained numerous RHI scans in every storm. RHIs of the radial velocity field frequently indicated air rising over the windward slope of the

Olympic Mountains beginning its rise well ahead of the mountains (Fig. 14), consistent with the well-known fact that the effect of mountains can be felt upwind (e.g., Grossman and Durran 1984; Houze et al. 2001; Houze 2014, chapter 12). RHIs of Doppler velocity spectrum width show high values in regions of strong wind shear. Figure 15 shows an example of

enhanced spectrum width that suggests the presence of Kelvin–Helmholtz (KH) waves in a layer of strong shear atop the low-level jet approaching the windward side of the mountains. The small-scale braided appearance in spectrum width data is a classic signature of KH waves (Chapman and Browning 1997; Medina and Houze 2016).

The nearly continuously available dual-polarization radar RHIs provided high-resolution information on precipitation microphysics. Figure 16 shows a frequently observed dual-polarization signal seen in OLYMPEX. The differential reflectivity (ZDR) is higher when particles tend to be horizontally oriented. Large values of ZDR are associated with the melting layer (~1.5 km in Fig. 16), which typically contains large oblate melting aggregates of ice particles, a primary signature of stratiform precipitation (amplified by the high dielectric constant of the melting particles). The secondary maximum of ZDR at 4–5-km altitude in Fig. 16 is a feature often seen in frontal systems moving over West Coast mountains (Kingsmill et al. 2006; Medina et al. 2007). It occurs about 2 km above the melting layer in the temperature range (−10° to −15°C) in which platelike crystals, including branched crystals such as dendrites, are expected (Houze 2014, chapter 6; Kennedy and Rutledge 2011; Schneebeli et al. 2013).

The Ka-/Ku-band dual-frequency D3R radar has especially high resolution and sensitivity. These

frequencies are the same as the DPR on GPM and enable the observation of both cloud and precipitation

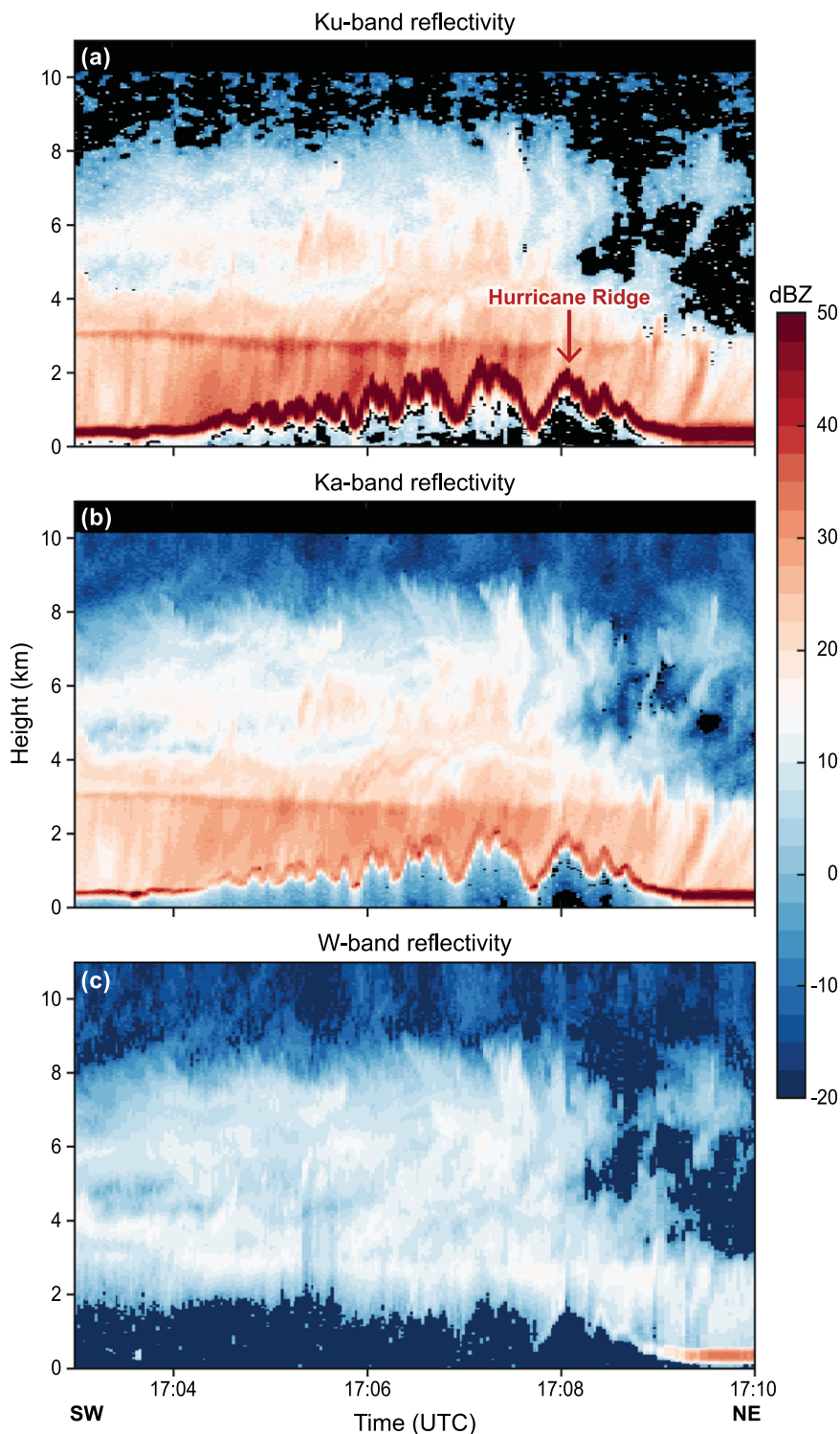


FIG. 13. Down-looking APR-3 radar data as the DC-8 flew southwest (left side) to northeast (right side) over the Olympic Mountains on 8 Dec 2015. The flight track was from the Pacific Ocean, over the Queets valley, over the high terrain and the Hurricane Ridge area, to the leeside of the mountains. Note that the radar reflectivity data have not yet been corrected for attenuation.

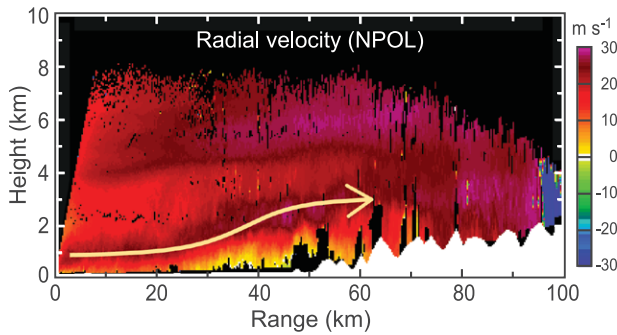


FIG. 14. Example of a radial velocity RHI over the Quinault valley from the NPOL at 0135 UTC 13 Nov 2015. The white region at the bottom of the cross section masks out the mountains. In this and subsequent NPOL figures, the quality-control process includes clutter removal. The data show a jet of cross-barrier flow rising over the terrain as indicated by the arrow.

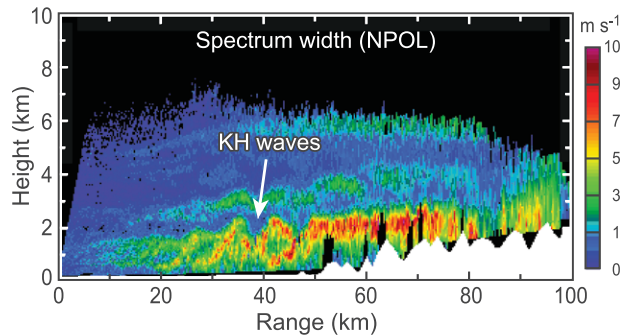


FIG. 15. Example of Doppler spectrum width RHI from the NPOL over the Quinault valley at 1936 UTC 5 Dec 2015. The white region at the bottom of the cross section masks out the mountains. The data show a classic pattern of Kelvin-Helmholtz waves in the low-level flow.

structures. The example in Fig. 17 illustrates the return from a postfrontal rain shower at Ka-band frequency. It shows narrow embedded pockets of reflectivity of 30–40 dBZ (~0.5 km in horizontal dimension) in the 5–10-km range and anvils with reflectivity from ~–10 to –20 dBZ at the 4–5-km level outside that range. This is the most detailed view yet of postfrontal convection of West Coast storms. It is well known to weather and avalanche forecasters in the Pacific Northwest that postfrontal cells significantly contribute to snow accumulation in the Olympic Mountains (see, e.g., Mass 2008).

The data obtained at the ground sites in Fig. 2 are critical to analyzing the nature of the precipitation observed in OLYMPEX. Figure 18 shows a time series of precipitation characteristics at one location at 285-m altitude in the Quinault valley from a Parsivel-2 and an MRR. The overprinted numbers and

arrows indicate five time periods of differing drop characteristics. By comparing the information in the four panels, we see that period 1 was characterized by uniformly tiny drops, low rain rates, and low fall velocity (1–3 m s^{–1}). Periods 2 and 4 had higher rain rates, and a large fraction of the rain rates were from larger drops with fall velocities of 5–6 m s^{–1}. During these periods, melting ice particles produced by deeper clouds probably accounted for the rain, with possible growth by scavenging of smaller drops at low levels; the reflectivity panel indicates increasing reflectivity with decreasing altitude, consistent with such scavenging. Periods 3 and 5 had a mix of drop sizes and rain rates, but much of the rain was accounted for by small drops, indicating a smaller proportion of water being collected by melted ice particles. The statistics of similar surface observations obtained in all OLYMPEX storms are a unique

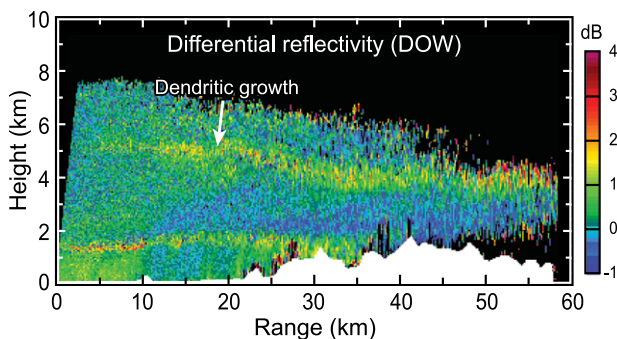


FIG. 16. Example of a differential reflectivity vertical RHI over the Quinault valley from the DOW radar at 0914 UTC 8 Dec 2015. The white region at the bottom of the cross section masks out the mountains. The data show a melting layer between 1- and 2-km altitude and a secondary maximum at 4–5 km.

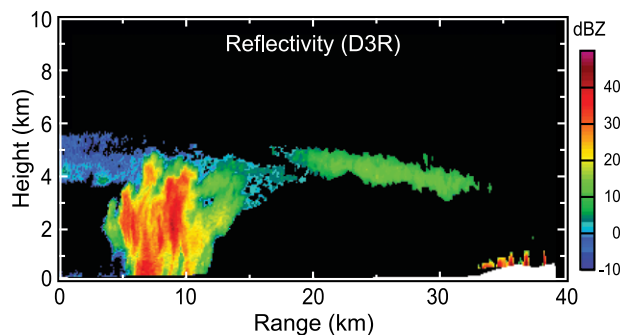


FIG. 17. Example of an RHI of Ka-band reflectivity observed by the D3R radar in an azimuth directed from the coast (range 0 km) toward the Quinault valley at 1828 UTC 18 Dec 2015.

resource for determining the nature of the precipitation processes and their orographic enhancement over windward slopes.

On the lee side, a more sophisticated PIP instrument was located at Hurricane Ridge under the RHI sector of the EC X-band radar (Fig. 19). As is the case of the other disdrometers the PIP can distinguish between rain and snow using hydrometeor fall speed, but the PIP provides more robust imaging and could operate in strong winds. These measurements are especially important because they were the only ground measurements obtained on the lee side of the Olympic Mountains. They will be used to differentiate between snow characteristics on the windward and lee sides. As can be seen in Fig. 19a, these measurements were made directly under the beam of the EC X-band radar on Vancouver Island.

The ice particle sizes and concentrations found aloft are especially important in algorithms for converting GPM measurements to precipitation rates. The Citation aircraft's state-of-the-art probes provided this information in-cloud. This aircraft repeatedly executed spiral ascents and descents in range of the NPOL and DOW radars, thus giving vertical profiles of ice particle sizes and concentrations to analyze in the context of dual-polarization radar data such as that in Fig. 16. The example of Citation data in Fig. 20 illustrates the comprehensive sampling ice particle

concentrations at temperatures below 0°C obtained during one spiral ascent. This particular profile was obtained near the DOW radar. Numerous other

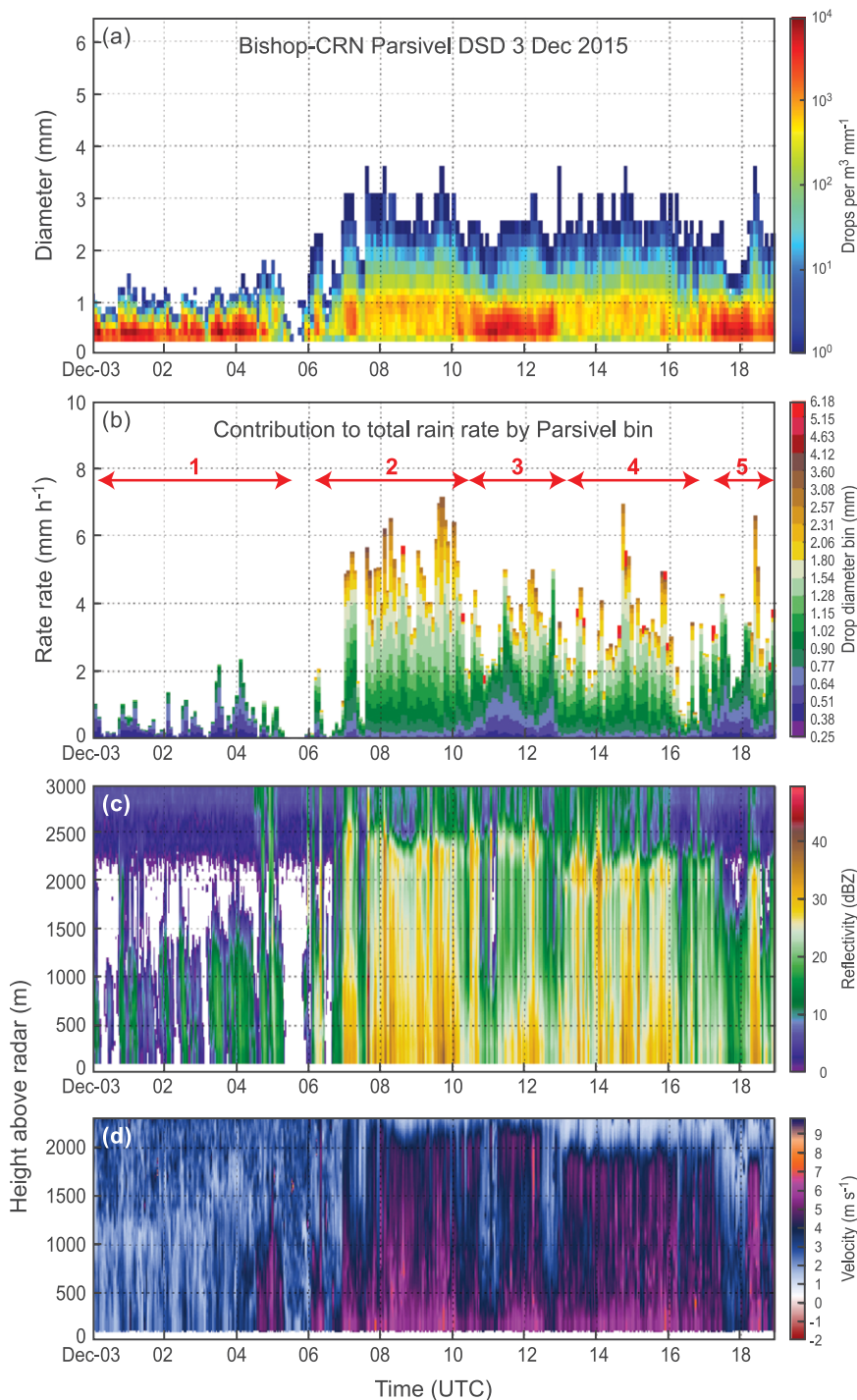


FIG. 18. Time series of ground instrument observations from the Bishop Field (CRN) site at 285-m altitude in the Quinault valley for the period 0000–1900 UTC 3 Dec 2015. (a) Parsivel-2 drop size distribution, (b) contribution to total rain rate by Parsivel drop size bin, (c) MRR reflectivity, and (d) MRR fall velocity. The red arrows in (b) highlight five periods of differing drop size distribution characteristics that are discussed in the text.

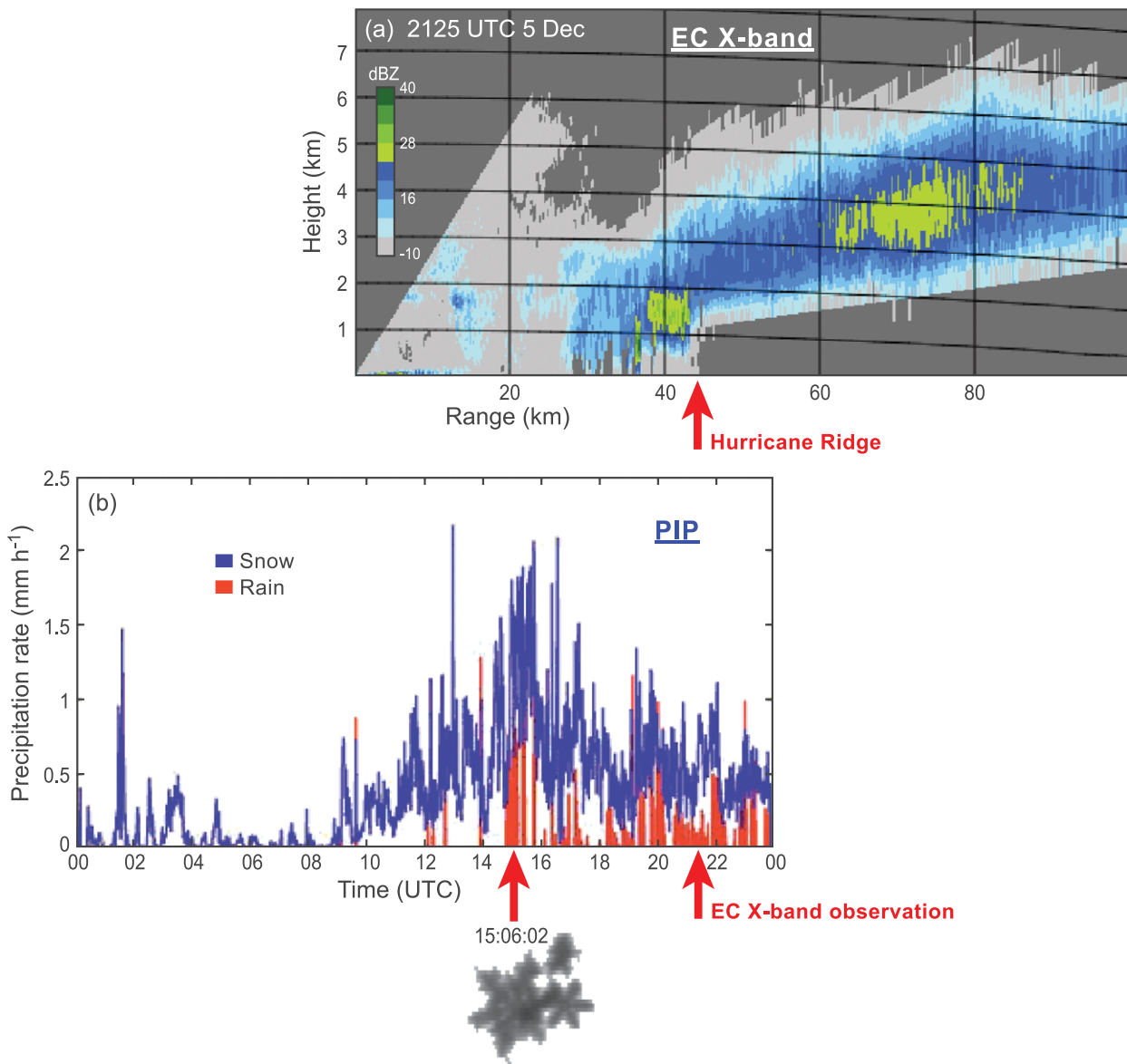


FIG. 19. (a) Reflectivity RHI from the EC X-band radar at Albert Head, Vancouver Island. The azimuth of the RHI points to the south over Hurricane Ridge. Beyond Hurricane Ridge, the beam is blocked by terrain. (b) Precipitation rates from the PIP at Hurricane Ridge. An example of snow particle images recorded by the PIP at the indicated time is shown.

in-cloud ascents and descents above the 0°C level were obtained near both DOW and NPOL, will be the basis for improved GPM algorithms, and can be compared to model simulations to determine if the ice-phase microphysics are being handled correctly in extratropical cyclones passing over complex terrain. The Citation flew almost exclusively on the windward side of the Olympic Range, and the microphysical samples included ice particle imagery (not shown), so the particle types and characteristics seen in these flights on the windward side can be compared to the particle characteristics seen on the lee side at Hurricane Ridge (e.g., Fig. 19).

SEASONAL STATISTICS: SNOW ACCUMULATION OVER THE OLYMPIC MOUNTAINS. The data obtained in OLYMPEX have statistical as well as case-study value. Not only will the aircraft, radar, and surface data described above be useful in understanding the behavior of individual storms, they provide statistics of the vertical structure of precipitating cloud systems that affect the West Coast during the wet season and document the accumulation of precipitation during that period. One of the goals of OLYMPEX was to track the growth and decline of snowpack in the Olympic Mountains. An example of a seasonal

time series of snow depth as measured at one of the snow pole sites is given in Fig. 21. The snow depth estimates from the two ASO flights, which agree well with the snow pole estimates, are also indicated on the figure. There were two major periods of snowpack accumulation, the latter half of December and during the month of March. Melt-off of the snow commenced at the end of March and early April. Further analysis of the snow pole data at all the sites and how they compare to different model estimates of snowpack accumulation and snow water equivalent during the 2015–16 water year are found in *Currier et al. (2017)*.

CONCLUSIONS. OLYMPEX is the most recent field experiment to study storms passing over West Coast mountain ranges of the Americas. The weather cooperated by providing a large representative sample of storms under both warm and cold conditions. Several precipitation events were of the “atmospheric river” type in which a long fetch of warm-sector water vapor influx impacted the Olympic Mountains, while others were dominated by warm-/cold-frontal dynamics or unstable post-frontal conditions. The OLYMPEX dataset will serve both NASA’s need for validation of its satellite-based precipitation retrieval algorithms over mountainous terrain and the more general need to advance our fundamental understanding of the physics and dynamics of frontal and orographic precipitation processes.

The instrumentation in OLYMPEX was unprecedented. The NASA DC-8 and ER-2 aircraft used radar and passive microwave remote sensors to view storms from above, in ways that are comparable to the sensors on the GPM satellite. With their long flight durations, these aircraft allowed processes to be sampled upwind, on the windward slopes, over the high terrain, and in the lee of the Olympic Mountains. Four scanning dual-polarization Doppler radars

were deployed to observe the precipitation upwind of, over, and downwind of the mountains. These radars were operated in RHI sector mode to optimize the vertical resolution and thus map comprehensively kinematic and microphysical processes. WSR-88Ds at Langley Hill and Camano Island, Washington, provided horizontal context for the specialized research radars. Soundings were enhanced with frequent launches at three sites and by dropsondes from the DC-8. The UND Citation aircraft sampled the precipitation particles in situ in a variety of flight tracks, including ascending and descending spirals. The Citation data provide verification of assumptions used to interpret the fields of microphysical parameters from the scanning radars. The precipitation arriving at the ground was documented by deploying surface stations at several altitudes within the area of scanning radar coverage on the windward and lee sides of the Olympic Mountains. The instrumentation at these sites sampled the precipitation rate, particle size distributions, and fall velocities of the precipitation particles. The snowpack in the Olympic Mountains was monitored over the entire fall–winter–spring wet season by snow cameras, ground crews, and lidar and spectrometer aboard the NASA ASO aircraft. This snowpack monitoring, together with the

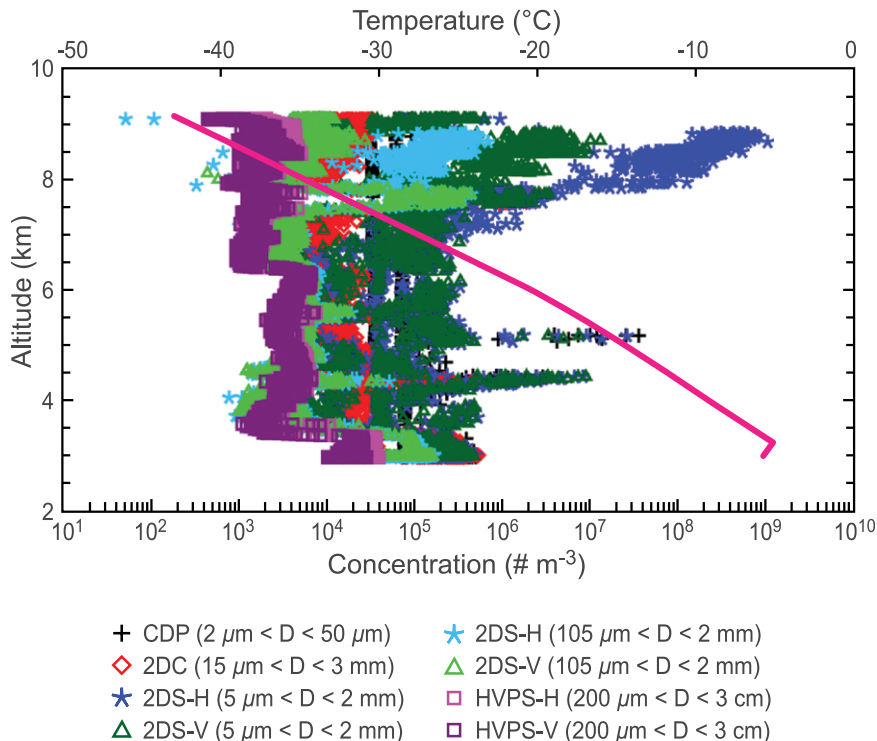


FIG. 20. Example of Citation data obtained 1459–1530 UTC 5 Dec 2015 as the aircraft spiraled upward through cloud. Concentrations of ice particles in different size ranges are shown as a function of altitude. Temperature as a function of altitude is shown by the pink line.

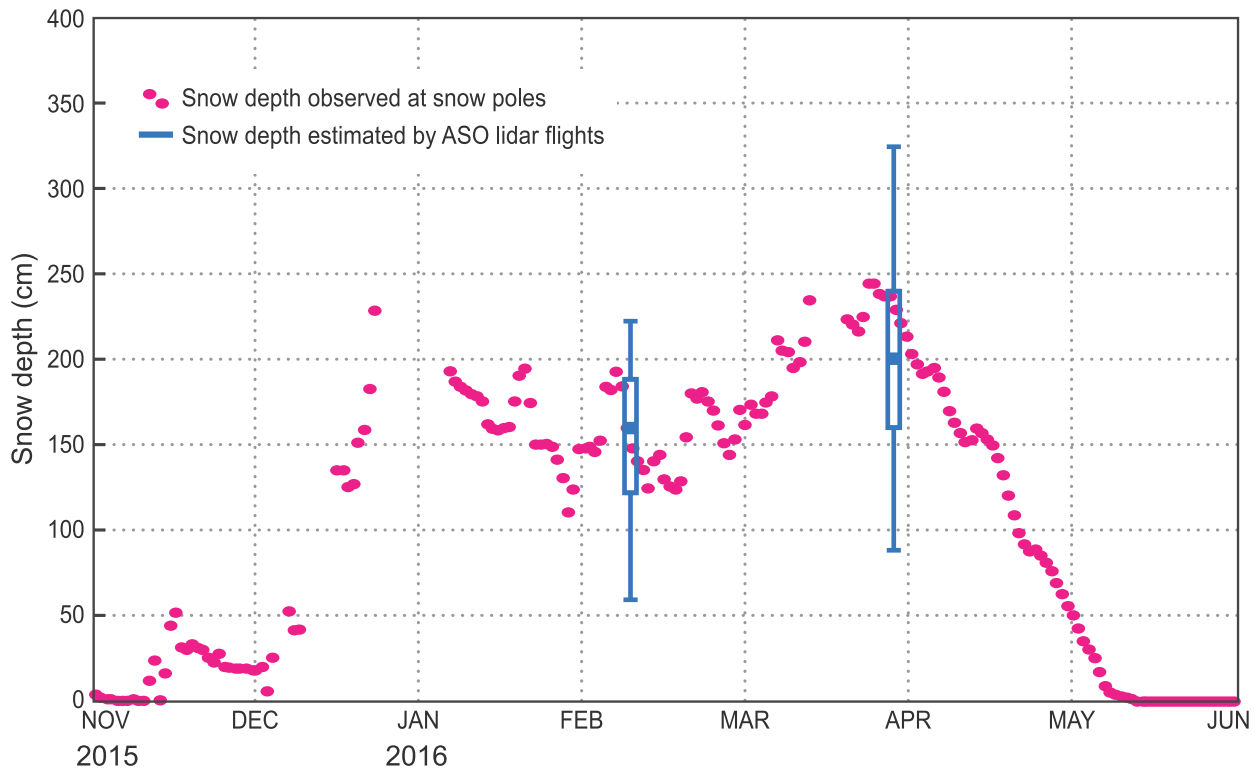


FIG. 21. Seasonal snow depth as measured at one of the snow poles (pink dots) located at 1301-m elevation near Mount Seattle (red triangle in Fig. 2) and two estimates of the snow depth by the ASO lidar flights made on 8–9 Feb and 29–30 Mar 2016 (blue box and whiskers). The lidar measurements are valid over a 60-m bounding area at the Mount Seattle location, the blue boxes on the plot enclose the first and third quartiles of the snow depth estimates, and the lowest and highest points outside each box are the lowest 10% and 90% snow depth values, respectively, within the 60-m area. Gaps in the snow-pole depth measurements are due to uncertainties when the camera lens was blocked or the snow depth was uneven around the pole. The vertical grid lines represent the beginning of each month. Figure adapted from Currier et al. (2017).

precipitation gauge measurements at multiple elevations, allows the individual storms of OLYMPEX to be considered in a broader season-long perspective. The OLYMPEX dataset is available to all investigators and is being archived by the Global Hydrology Research Center located at NASA's Marshall Space Flight Center. (Please see <https://ghrc.nsstc.nasa.gov/home/> and <http://olympex.atmos.washington.edu> for more information.)

ACKNOWLEDGMENTS. In addition to the authors of this paper, the following individuals had leadership roles in OLYMPEX. For flight operations: S. Braun, D. Cecil, A. Didlake, S. L. Durden, T. L'Ecuyer, T. Lang, R. Marchand, G. McFarquhar, J. Munchak, S. Nesbitt, J. Nystrom, and E. Zipser. Radar operations: D. Wolf, P. Rodriguez, V. Chandrasekar, J. Wurman, K. Kosiba, and M. Watson. Ground sites: M. Wingo and C. Urnes. Sounding support: P. Cieselski and T. Hock. Forecasting: T. Alvey, S. Bang, N. Weber, P. Veals, and L. Campbell. Information technology (IT) and data support: S. Brodzik and M. Dixon. Snow observations:

W. R. Currier, J. Pflug, and T. Thorson. Public relations: D. Kirschbaum. Media support and logistics: S. O'Donnell. B. Tully designed the OLYMPEX logo and provided graphics and editorial support. Over 100 other individuals were key in making OLYMPEX successful, especially the aircraft crews, radiosonde launchers, airborne instrument operators and engineers, ground radar engineers and operators, crews maintaining surface sites, employees and contractors of the National Park Service, the U.S. Forest Service, the U.S. Fish and Wildlife Service, and officials of the Quinault Indian Nation. University of Washington participants have been supported for OLYMPEX by NASA Grants NNX12AL54G, NNX13AO58G, NNX14AJ72G, NNX14AO64G, NNX15AL38G, NNX15AT26G, NNX16AD75G, and NNX16AK05G and NSF Grant AGS-1503155. The participation of the ER-2 aircraft and the AMPR instrument on the DC-8 were funded by NASA's Aerosols/Clouds/Ecosystems (A/C/E) 2007 Decadal Survey Study as part of its Radar Definition Experiment (RADEX 2015) activities. Robert Houze was partly supported by the U.S. Department of Energy (DOE) Office of Science Biological

and Environmental Research (BER) as part of the Regional and Global Climate Modeling Program and Northwest National Laboratory (PNNL) under Task Order 292896 (WACCEN) of Master Agreement 243766. PNNL is operated for DOE by Battelle Memorial Institute under Contract DE-AC05-76RL01830. W. Petersen was supported by the National Aeronautics and Space Administration GPM and PMM Programs. S. Tanelli's work was performed at the Jet Propulsion Laboratory, California Institute of Technology, under contract with National Aeronautics and Space Administration. Airborne lidar imagery was obtained by the NASA Jet Propulsion Laboratory Airborne Snow Observatory, funded by NASA's Terrestrial Hydrology Program. We especially thank Vaisala Inc., who took quick action to replace a stolen radiosonde unit just prior to the start of OLYMPEX.

REFERENCES

- Chapman, D., and K. A. Browning, 1997: Radar observations of wind-shear splitting within evolving atmospheric Kelvin-Helmholtz billows. *Quart. J. Roy. Meteor. Soc.*, **123**, 1433–1439, doi:10.1002/qj.49712354114.
- Currier, W. R., T. Thorson, and J. D. Lundquist, 2017: Independent evaluation of frozen precipitation from WRF and PRISM in the Olympic Mountains, WA, USA. *J. Hydrometeorol.*, doi:10.1175/JHM-D-17-0026.1, in press.
- Grossman, R. L., and D. R. Durran, 1984: Interaction of low-level flow with the Western Ghats Mountains and offshore convection in the summer monsoon. *Mon. Wea. Rev.*, **112**, 652–672, doi:10.1175/1520-0493(1984)112<0652:IOLLFW>2.0.CO;2.
- Hou, A. Y., and Coauthors, 2014: The Global Precipitation Measurement mission. *Bull. Amer. Meteor. Soc.*, **95**, 701–722, doi:10.1175/BAMS-D-13-00164.1.
- Houze, R. A., Jr., 2012: Orographic effects on precipitating clouds. *Rev. Geophys.*, **50**, RG1001, doi:10.1029/2011RG000365.
- , 2014: *Cloud Dynamics*. 2nd ed. Elsevier/Academic Press, 432 pp.
- , and P. V. Hobbs, 1982: Organization and structure of precipitating cloud systems. *Advances in Geophysics*, Vol. 28, Academic Press, 225–315, doi:10.1016/S0065-2687(08)60521-X.
- , —, K. R. Biswas, and W. M. Davis, 1976: Mesoscale rainbands in extratropical cyclones. *Mon. Wea. Rev.*, **104**, 868–878, doi:10.1175/1520-0493(1976)104<0868:MRIEC>2.0.CO;2.
- , C. N. James, and S. Medina, 2001: Radar observations of precipitation and airflow on the Mediterranean side of the Alps: Autumn 1998 and 1999. *Quart. J. Roy. Meteor. Soc.*, **127**, 2537–2558, doi:10.1002/qj.49712757804.
- , K. L. Rasmussen, M. D. Zuluaga, and S. R. Brodzik, 2015: The variable nature of convection in the tropics and subtropics: A legacy of 16 years of the Tropical Rainfall Measuring Mission (TRMM) satellite. *Rev. Geophys.*, **53**, 994–1021, doi:10.1002/2015RG000488.
- Huffman, G. J., and Coauthors, 2007: The TRMM Multisatellite Precipitation Analysis (TMPA): Quasi-global, multiyear, combined-sensor precipitation estimates at fine scales. *J. Hydrometeorol.*, **8**, 38–55, doi:10.1175/JHM560.1.
- Kalnay, E., and Coauthors, 1996: The NCEP/NCAR 40-Year Reanalysis Project. *Bull. Amer. Meteor. Soc.*, **77**, 437–471, doi:10.1175/1520-0477(1996)077<0437:TNYRP>2.0.CO;2.
- Kennedy, P. C., and S. A. Rutledge, 2011: S-band dual-polarization radar observations of winter storms. *J. Appl. Meteor. Climatol.*, **50**, 844–858, doi:10.1175/2010JAMC2558.1.
- Kingsmill, D. E., P. J. Neiman, F. M. Ralph, and A. B. White, 2006: Synoptic and topographic variability of northern California precipitation characteristics in landfalling winter storms observed during CALJET. *Mon. Wea. Rev.*, **134**, 2072–2094, doi:10.1175/MWR3166.1.
- Kummerow, C., W. Barnes, T. Kozu, J. Shiue, and J. Simpson, 1998: The Tropical Rainfall Measuring Mission (TRMM) sensor package. *J. Atmos. Oceanic Technol.*, **15**, 809–816, doi:10.1175/1520-0426(1998)015<0809:TTRMMT>2.0.CO;2.
- Marwitz, J. D., 1987: Deep orographic storms over the Sierra Nevada. Part I: Thermodynamic and kinematic structure. *J. Atmos. Sci.*, **44**, 159–173, doi:10.1175/1520-0469(1987)044<0159:DOSOTS>2.0.CO;2.
- Mass, C., 2008: *Weather of the Pacific Northwest*. University of Washington Press, 280 pp.
- Matejka, T. J., R. A. Houze Jr., and P. V. Hobbs, 1980: Microphysics and dynamics of clouds associated with mesoscale rainbands in extratropical cyclones. *Quart. J. Roy. Meteor. Soc.*, **106**, 29–56, doi:10.1002/qj.49710644704.
- Medina, S., and R. A. Houze Jr., 2016: Kelvin-Helmholtz waves in extratropical cyclones passing over mountain ranges. *Quart. J. Roy. Meteor. Soc.*, **142**, 1311–1319, doi:10.1002/qj.2734.
- , E. Sukovich, and R. A. Houze Jr., 2007: Vertical structures of precipitation in cyclones crossing the Oregon Cascades. *Mon. Wea. Rev.*, **135**, 3565–3586, doi:10.1175/MWR3470.1.
- Minder, J. R., D. R. Durran, G. H. Roe, and A. M. Anders, 2008: The climatology of small-scale orographic precipitation over the Olympic Mountains:

- Patterns and processes. *Quart. J. Roy. Meteor. Soc.*, **134**, 817–839, doi:10.1002/qj.258.
- , —, and —, 2011: Mesoscale controls on the mountainside snow line. *J. Atmos. Sci.*, **68**, 2107–2127, doi:10.1175/JAS-D-10-05006.1.
- Nagle, R. E., and S. M. Serebreny, 1962: Radar precipitation echo and satellite cloud observations of a maritime cyclone. *J. Appl. Meteor.*, **1**, 279–295, doi:10.1175/1520-0450(1962)001<0279:RPEASC>2.0.CO;2.
- Neiman, P. J., F. M. Ralph, G. A. Wick, J. D. Lundquist, and M. D. Dettinger, 2008: Meteorological characteristics and overland precipitation impacts of atmospheric rivers affecting the west coast of North America based on eight years of SSM/I satellite observations. *J. Hydrometeor.*, **9**, 22–47, doi:10.1175/2007JHM855.1.
- Painter, T. H., and Coauthors, 2016: The Airborne Snow Observatory: Fusion of scanning lidar, imaging spectrometer, and physically-based modeling for mapping snow water equivalent and snow albedo. *Remote Sens. Environ.*, **184**, 139–152, doi:10.1016/j.rse.2016.06.018.
- Schneebeil, M., N. Dawes, M. Lehning, and A. Berne, 2013: High-resolution vertical profiles of X-Band polarimetric radar observables during snowfall in the Swiss Alps. *J. Appl. Meteor. Climatol.*, **52**, 378–394, doi:10.1175/JAMC-D-12-015.1.
- Simpson, J., 1988: TRMM: A satellite mission to measure tropical rainfall. National Aeronautics and Space Administration Science Steering Group Rep., 94 pp.
- , C. Kummerow, W.-K. Tao, and R. F. Adler, 1996: On the Tropical Rainfall Measuring Mission (TRMM). *Meteor. Atmos. Phys.*, **60**, 19–36, doi:10.1007/BF01029783.
- Skamarock, W. C., and Coauthors, 2008: A description of the Advanced Research WRF version 3. NCAR Tech. Note NCAR/TN-475+STR, 125 pp., doi:10.5065/D68S4MVH.
- Zipser, E. J., D. J. Cecil, C. Liu, S. W. Nesbitt, and D. P. Yorty, 2006: Where are the most intense thunderstorms on Earth? *Bull. Amer. Meteor. Soc.*, **87**, 1057–1071, doi:10.1175/BAMS-87-8-1057.

NEW FROM AMS BOOKS!

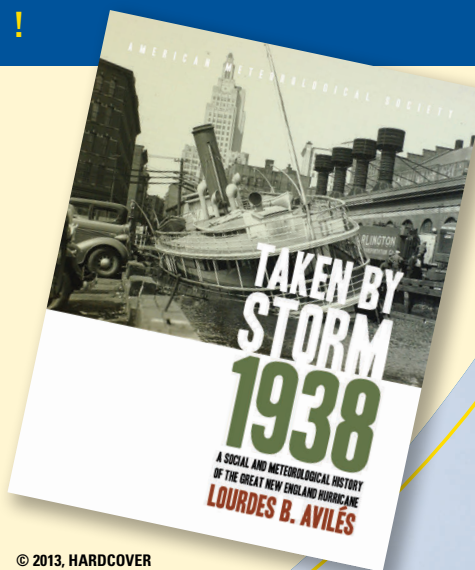
“An engrossing account of New England’s worst natural catastrophe.”

— KERRY EMANUEL, *Professor of Atmospheric Science, MIT*

Taken by Storm, 1938: *A Social and Meteorological History of the Great New England Hurricane*

LOURDES B. AVILÉS

When the Great New England Hurricane of 1938 hit the Northeast unannounced, it changed everything from the landscape, to Red Cross and Weather Bureau protocols, to the measure of Great Depression relief New Englanders would receive, and the resulting pace of regional economic recovery. The science behind this storm is presented here for the first time, with new data that sheds light on the motivations of the Weather Bureau forecasters. This compelling history successfully weaves science, historical accounts, and social analyses to create a comprehensive picture of the most powerful and devastating hurricane to hit New England to date.



© 2013, HARDCOVER
ISBN: 978-1-878220-37-0
LIST \$40 MEMBER \$30

AMS BOOKS

RESEARCH APPLICATIONS HISTORY

www.ametsoc.org/amsbookstore